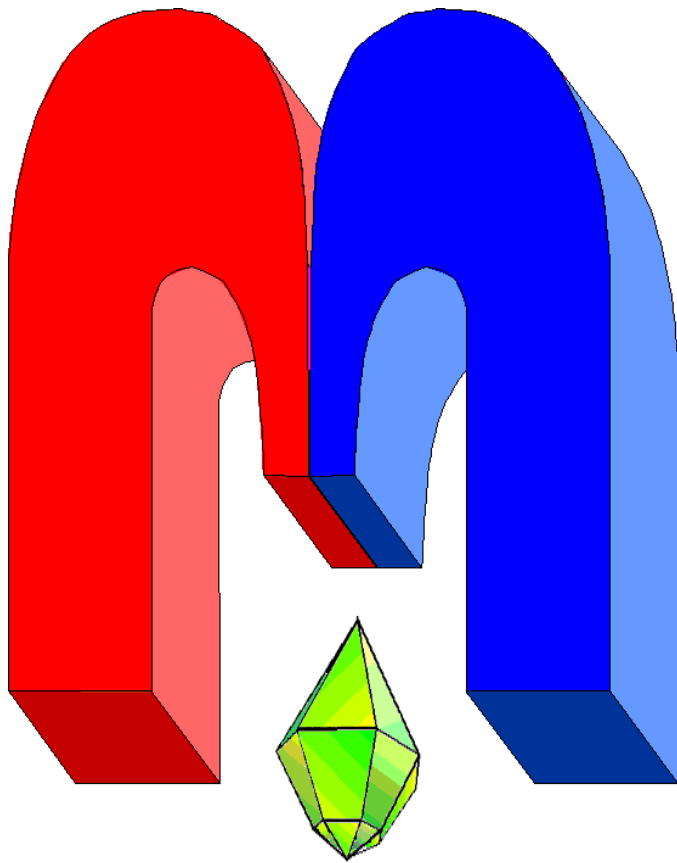


ISSN 2072-5981
doi: 10.26907/mrsej



***magnetic
Resonance
in Solids***

Electronic Journal

Volume 21

Issue 5

Paper No 19505

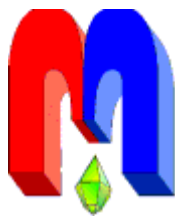
1-16 pages

2019

doi: [10.26907/mrsej-19505](https://doi.org/10.26907/mrsej-19505)

<http://mrsej.kpfu.ru>

<http://mrsej.ksu.ru>



Established and published by Kazan University
Endorsed by International Society of Magnetic Resonance (ISMAR)
Registered by Russian Federation Committee on Press (#015140),
August 2, 1996
First Issue appeared on July 25, 1997

© Kazan Federal University (KFU)*

"Magnetic Resonance in Solids. Electronic Journal" (MRSej) is a peer-reviewed, all electronic journal, publishing articles which meet the highest standards of scientific quality in the field of basic research of a magnetic resonance in solids and related phenomena.

Indexed and abstracted by
Web of Science (ESCI, Clarivate Analytics, from 2015), Scopus (Elsevier, from 2012), RusIndexSC (eLibrary, from 2006), Google Scholar, DOAJ, ROAD, CyberLeninka (from 2006), SCImago Journal & Country Rank, etc.

Editor-in-Chief

Boris Kochelaev (KFU, Kazan)

Honorary Editors

Jean Jeener (Universite Libre de Bruxelles, Brussels)
Raymond Orbach (University of California, Riverside)

Executive Editor

Yurii Proshin (KFU, Kazan)
mrsej@kpfu.ru



This work is licensed under a [Creative Commons Attribution-ShareAlike 4.0 International License](https://creativecommons.org/licenses/by-sa/4.0/).



This is an open access journal which means that all content is freely available without charge to the user or his/her institution. This is in accordance with the [BOAI definition of open access](https://www.boai.ru/).

Technical Editor

Maxim Avdeev (KFU, Kazan)

Editors

Vadim Atsarkin (Institute of Radio Engineering and Electronics, Moscow)

Yurij Bunkov (CNRS, Grenoble)

Mikhail Eremin (KFU, Kazan)

David Fushman (University of Maryland, College Park)

Hugo Keller (University of Zürich, Zürich)

Yoshio Kitaoka (Osaka University, Osaka)

Boris Malkin (KFU, Kazan)

Alexander Shengelaya (Tbilisi State University, Tbilisi)

Jörg Sichelschmidt (Max Planck Institute for Chemical Physics of Solids, Dresden)

Haruhiko Suzuki (Kanazawa University, Kanazawa)

Murat Tagirov (KFU, Kazan)

Dmitrii Tayurskii (KFU, Kazan)

Valentine Zhikharev (KNRTU, Kazan)

* In Kazan University the Electron Paramagnetic Resonance (EPR) was discovered by Zavoisky E.K. in 1944.

Calculation of single crystal and polycrystalline pulsed EPR signals including relaxation by phonon modulation of hyperfine and \tilde{g} matrices by solving Liouville-von Neumann equation

S.K. Misra*, H.R. Salahi, L. Li

Physics Department, Concordia University, 1455 de Maisonneuve Boulevard West,
Montreal, Quebec H3G 1M8, Canada

**E-mail: sushil.misra@concordia.ca*

(Received August 15, 2019; revised September 17, 2019;
accepted September 24, 2019; published October 17, 2019)

Liouville-von Neumann equation has been solved numerically to calculate pulsed electron paramagnetic resonance (EPR) signals rigorously in Liouville space taking into account relaxation by spin-phonon modulation of hyperfine and \tilde{g} tensors in single crystal and polycrystalline materials. It is illustrated here for a spin-coupled electron-nuclear system with the electron spin $S = 1/2$ and nuclear spin $I = 1/2$ to calculate the spin echo correlation spectroscopy (SECSY) and echo-electron-electron double-resonance (echo-ELDOR) signals. Both a single-crystal spectrum for a chosen orientation of the external magnetic field with respect to the crystal axes and powder spectrum can be calculated. The flow chart for the simulation is included. The calculations can be carried out on a PC using Matlab within a reasonable time. A software has been developed in Matlab to do these calculations, which only requires to input the parameters on a laptop equipped with Matlab software.

PACS: 76.30.-v, 76.70.Dx

Keywords: pulsed EPR, two-dimensional spin-echo-correlation spectroscopy (2D-SECSY), two-dimensional electron-electron double-resonance (2D-ELDOR), Liouville-von Neumann equation

1. Introduction

Two dimensional Fourier transform (FT)-pulsed EPR (Electron Paramagnetic Resonance; also known as ESR: Electron Spin Resonance) experiments are useful in studying nuclear modulation and relaxation effects, among others. Whereas both spin echo correlation spectroscopy (SECSY) and echo-electron-electron double-resonance (echo-ELDOR) can be used to study the effect of nuclear modulation on pulsed EPR signals, echo-ELDOR can, in addition, resolve better the cross peaks due to exchange and nuclear modulation because of the extra provision of mixing time, T_m , in the pulse sequence. One such study was reported by Lee, Patyal and Freed [1] (hereafter LPF) on a γ -irradiated single crystal of malonic acid. This was a prototype study to demonstrate the capabilities of two-dimensional (2D)-FT-ESR experiments in the study of nuclear modulation. Single crystals are ideal systems to check the validity of experimental approaches and accuracy of theoretical models. This objective was accomplished reasonably well in [1]. However, the effects of static Hamiltonian and relaxation during the pulse were not taken into account, and the calculations were not carried out for a polycrystalline (also referred to as powder) material, which is the most often encountered situation since single crystals are not always available. In order to take into account relaxation rigorously, it is imperative to solve Liouville-von Neumann (LVN) equation, which is an exact quantum mechanical equation of motion for the density matrix in Liouville space. The density matrix in Hilbert space in a chosen basis set is written in vector form as a single column by stacking the successive columns on the top of each other, the first column being on the top. The LVN equation is valid even for

relatively slow random processes, and is therefore especially suitable for EPR, where the natural time scale is short so that the random processes do not usually appear fast on this time scale. A numerical simulation technique for calculating electron-nuclear spin-echo signals detected in pulsed EPR experiments has been developed here. It is based on solving LVN equation, including relaxation. It is the purpose of this paper to extend the calculations of [1] to a polycrystalline (powder) sample, treating relaxation rigorously and including the static Hamiltonian during pulses, using the LVN equation.

2. Theoretical background

The LVN equation considered here is time-independent, but includes a relaxation term, and a time-dependent, but not in a stochastic fashion, that represents the pulses. The algorithm used to compute the SECSY and echo-ELDOR spectra is outlined as follows. For more details of the procedure used, see Misra and Li [2] (hereafter ML). The time evolution of the spin density matrix, $\rho(t)$, taking into account relaxation effects, is governed by the Liouville-von Neumann (LNV) equation [1, 3–7]:

$$\frac{d}{dt}\hat{\rho}(t) = -i\hat{H}\hat{\rho}(t) - \hat{\Gamma}(\hat{\rho}(t) - \hat{\rho}_0), \quad (1)$$

where $\hat{H}\hat{\rho}(t) \equiv [\hat{H}, \hat{\rho}(t)]$, $\hat{\Gamma}$ is the relaxation superoperator and $i^2 = -1$. Since ρ_0 is time independent, Eq. (1) can be written as

$$\frac{d}{dt}\hat{\chi}(t) = -i\hat{H}\hat{\chi}(t) - \hat{\Gamma}\hat{\chi}(t), \quad (2)$$

where $\chi(t) = \rho(t) - \rho_0$ is the reduced density matrix. In Eq.(1), $\hat{H} = \hat{H}_0 + \hat{H}_1$ is the Hamiltonian operator, where \hat{H}_0 and \hat{H}_1 are its time-independent (static Hamiltonian) and time-dependent (pulse) parts, respectively; $\hat{\Gamma}$ the relaxation superoperator, and assumed to be time independent here. (Throughout the paper, the single and double carets, $\hat{}$ and $\hat{}$ will be used to denote the operators and the superoperators, respectively.) Equation (1) is an operator equation, which can be expressed as a matrix equation in a given set of operators $|i\rangle\langle j|$; $i, j = 1, 2, \dots, n$, where $|i\rangle$ are the eigenvectors of \hat{H}_0 . The coefficients, $\rho_{i,j}$, $H_{i,j}$ in the expansion of the operators $\hat{\rho}$ and \hat{H}_0 in this basis, respectively, are then used to write the corresponding matrix equation. More details of the eigenvectors and eigenvalues of \hat{H}_0 , as well the matrix representation for \hat{H}_1 for are given in Appendix A. The details of the relaxation matrix as described by Redfield [5] are given in Appendix B.

2.1. Initial density matrix

In Eq.(1), ρ_0 is the initial thermal equilibrium density matrix, governed by the Boltzmann distribution for an electron spin 1/2 in thermal equilibrium. Using high-temperature approximation and neglecting the energy-level modification by the hyperfine interaction which is much less than the electronic Zeeman interaction we can write:

$$\rho_0 = \frac{\exp(-\hbar\hat{H}/kT)}{\text{Tr}[\exp(-\hbar\hat{H}/kT)]} \propto \mathbb{1} - \frac{\hbar}{k_B T} S_z. \quad (3)$$

Since the final signal is obtained by taking the trace: $\text{Tr}(S_+ \rho_f)$ and during the evolution of ρ_0 to ρ_f the term $\mathbb{1}$ in Eq (3) remains invariant, it does not contribute to the signal as $\text{Tr}(S_+ \mathbb{1}) = 0$, one can thus choose

$$\rho_0 \propto S_z \quad (4)$$

for the present calculations. Here Z -axis is defined to be aligned along the direction of the external magnetic field. (It is noted here that Eq. (4) is only valid for spin $1/2$. However, for high spin quantum number systems $S > 1/2$, e.g. transition metal ions, characterized by zero-field splitting interactions, the initial density matrix is different from that given by Eq. (4). see e.g. [8, 9].)

2.2. Evolution of density matrix

Free evolution. As described by ML [2] in the absence of pulse (free evolution), the density matrix $\rho(t)$, expressed in Liouville space, becomes, after a period of time Δt :

$$\hat{\chi}(t + \Delta t) = e^{-\Delta t \hat{L}'} \hat{\chi}(t), \quad (5)$$

where

$$\hat{L}' \equiv i\hat{L} + \hat{\Gamma} \quad (6)$$

and the Liouvillian,

$$\hat{L} \equiv (I_n \otimes \hat{H} - \hat{H}^T \otimes I_n). \quad (7)$$

Here \otimes denotes direct product and I_n is the 2×2 unit matrix in the nuclear space. In what follows, $\rho(t)$ will be used instead of $\chi(t)$.

Action of a pulse. The density matrix under the action of a pulse, \hat{H}_1 , taking into account the static Hamiltonian H_0 becomes [2]

$$\hat{\rho}(t + \Delta t) = e^{-\Delta t (\hat{P} + \hat{\Gamma})} \hat{\rho}(t), \quad (8)$$

where the generalized pulse propagator, \hat{P} , including the static Hamiltonian, is

$$\hat{P} \equiv i[I_n \otimes (\hat{H}_1 + \hat{H}_0) - (\hat{H}_1 + \hat{H}_0)^T \otimes I_n]. \quad (9)$$

Numerical implementation of Eqs. (5) and (8) to compute pulsed EPR signals is outlined below in section 3.

2.3. Rotating frame

The calculations are carried out in the rotating frame in which the effective magnetic field $B_{\text{eff}} = (B - \hbar\omega/g\mu_B) = 0$. During the free evolution, in the absence of a pulse, one can still use the rotating-frame value $B = B_{\text{eff}} = 0$. Then the Zeeman term of the static Hamiltonian becomes zero both during, and in the absence of, a pulse.

3. Numerical computation of SECSY and echo-ELDOR pulsed-ESR signals

3.1. Pulse sequence

The pulse sequences and the relevant coherence pathways are shown in Figs. 1 and 2, respectively, for SECSY and echo-ELDOR computation [1, 10, 11]. In the calculation, one starts with the (un-normalized) initial density matrix in thermal equilibrium, as given by Eq. (4), for the electron spin $S = 1/2$. (The normalization is performed at the end of the calculation). The pulse sequence, as shown in Figs. 1 and 2, respectively, for SECSY and echo-ELDOR signals, transforms the initial density matrix under the successive action of pulses and subsequent free-evolutions.

During the pulse sequence, a k -th pulse is applied at the time t . It acts during the time, Δt , in the frame of reference rotating with the angular frequency of the circular component of

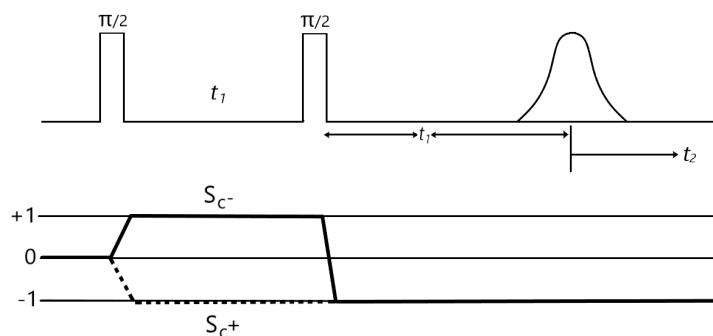


Figure 1. (Top) Pulse sequence for obtaining SECSY signal. The t_1 time between the two pulses and t_2 time from the echo are stepped. (Bottom) The coherence pathway S_{c-} used for calculating SECSY signal for an unpaired electron ($S = 1/2$) interacting with a single nucleus ($I = 1/2$) is shown by the solid line. Here p is the coherence order, which represents transverse magnetization, corresponding to spins rotating in a plane perpendicular to the external field [12].

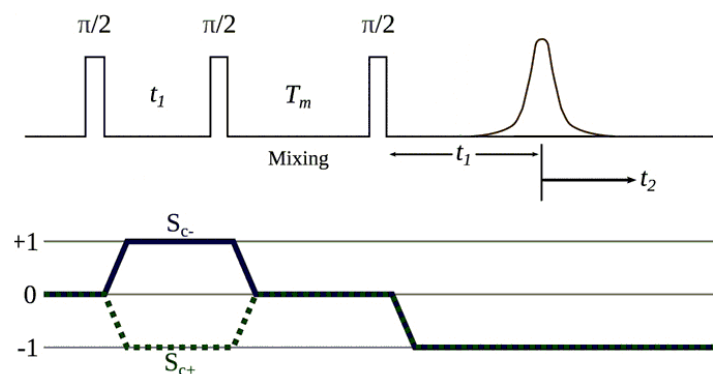


Figure 2. (Top) Pulse sequence for obtaining echo-ELDOR signal. The t_1 time between the first two pulses and t_2 time from the echo are stepped. Here T_m is the mixing time. (Bottom) The coherence pathways used for calculating 2D-ELDOR signal for an unpaired electron ($S = 1/2$) interacting with a single nucleus ($I = 1/2$) is shown by the solid line. Here p is the coherence order, which represents transverse magnetization, corresponding to the spins rotating in a plane perpendicular to the external field [12].

microwave magnetic field at the Larmor frequency of the electron spin. It transforms the density matrix, $\hat{\rho}(t)$, according to Eq. (8). The action of a pulse produces, in general, a change in the coherence order, p [12]. In order to follow the coherent pathway, p_k , of interest, the density matrix is then projected onto the coherence pathways p_k , which are chosen after the pulses according to Figs. 1 and 2, respectively, for SECSY and echo-ELDOR signals, as follows:

$$\hat{\rho}'(t + \Delta t) = P(p_k)\hat{\rho}(t + \Delta t), \quad (10)$$

where the idempotent operator $P(p_k)$ projects the density matrix on to the coherence pathways p_k to be followed after the k -th pulse. As shown in Figs. 1 and 2, the successive coherence pathways followed are $p = (1); (-1)$ and $p = (1); (0); (-1)$ for SECSY and echo-ELDOR, respectively for the respective S_{c-} pathways. More details of coherence pathways are given in Appendix C.

3.2. Free evolution

Subsequent to the action of a pulse, the free evolution during the time Δt transforms the density matrix according to Eq. (5).

3.3. The final density matrix (ρ_f)

Single crystal. For a single crystal, for the external field, B_0 , orientation at the angles (θ, ϕ) , where θ is the angle between B_0 and the z axis, and ϕ is the angle between the x axis and the projection of B_0 on the xy plane (see Fig. 3 below) ρ_f is a function of two times, t_1 and t_2 , which are stepped in the experiment, as seen from Figs. 1 and 2, respectively for SECSY and echo-ELDOR signals. The complex signal is

$$S(t_1, t_2, \theta, \phi) = \text{Tr}(S_+ \rho_f), \quad (11)$$

where $S_+ = S_x + iS_y$. The measured absorption signal is the imaginary part of $S(t_1, t_2, \theta, \phi)$ as given by Eq. (11).

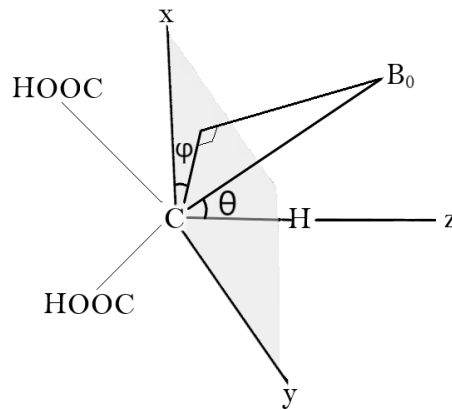


Figure 3. Relation of the principal axes (x, y, z) of the \tilde{g} , hyperfine matrices, assumed coincident to the structure of the malonic acid radical $\text{CH}(\text{COOH})_2$. Here, the z axis is along the C-H bond direction and the x axis is perpendicular to the plane of the three carbon atoms [13]. The direction of the external static field B_0 is defined by the angles θ and ϕ , where θ is the angle between B_0 and the z axis, and ϕ is the angle between the x axis and the projection of B_0 on the xy plane.

Polycrystalline (powder) sample. The echo signal for a polycrystalline (powder) sample is the average of the signals over the orientations (θ, ϕ) over the unit sphere of the molecule with respect to the external field, B_0 , in the laboratory frame (Fig. 3):

$$S_{\text{pdr}}(t_1, t_2) = \int_0^{2\pi} d\phi \int_0^{\pi} S(t_1, t_2, \theta, \phi) \sin(\theta) d\theta. \quad (12)$$

For powder average in an isotropic medium it suffices to set the integration limits to $[0, \pi/2]$ in the axial angle θ and $[0, \pi]$ in the azimuthal angle ϕ . The integral, as given by Eq. (12), is performed by a summation over the unit sphere over the angles (θ_j, ϕ_k) [14]:

$$S_{\text{pdr}}(t_1, t_2) = \sum_{\theta_j, \phi_k} S(t_1, t_2, \theta_j, \phi_k) \sin(\theta_j). \quad (13)$$

The Fourier transform, $S(\omega_1, \omega_2)$, of the imaginary part of $S(t_1, t_2)$ is the 2D-FT ESR signal.

As the static spin Hamiltonian as given in Eq. (A.2) in Appendix A is given in terms of the Euler angles (β, γ) rather than in terms of (θ, ϕ) , it will be easier to use (β, γ) instead of (θ, ϕ) . It is shown in Appendix D that if one were to use β, γ instead of θ, ϕ , respectively, the

polycrystalline integral given by Eq. (12) has the same value. Consequently, it is easier to use the integral

$$S_{\text{pdr}}(t_1, t_2) = \int_0^{2\pi} d\gamma \int_0^{\pi} S(t_1, t_2, \beta, \gamma) \sin(\beta) d\beta. \quad (14)$$

Accordingly, the summation (13) for the calculation presented here is changed to

$$S_{\text{pdr}}(t_1, t_2) = \sum_{\beta_j, \gamma_k} S(t_1, t_2, \beta_j, \gamma_k) \sin(\beta_j). \quad (15)$$

The flow chart for the calculation of pulsed signal is given in Appendix E.

3.4. Gaussian inhomogeneous broadening effect

In accordance with that used in LPF [1], the Gaussian inhomogeneous broadening effect in the frequency-domain along $\omega_2 (= 2\pi\nu)$, corresponding to the step time t_2 , (Figs. 1 and 2), is taken into account by the following time-domain dependence:

$$f_b(t_2) = f(t_2) \frac{1}{\sqrt{2\pi\Delta}} \int_{-\infty}^{\infty} \exp\left(\frac{-\nu^2}{2\Delta^2} - i2\pi\nu t_2\right) d\nu = f(t_2) e^{-2(\pi\Delta t_2)^2}, \quad (16)$$

where $f_b(t_2)$ is the Gaussian-broadened signal along t_2 and Δ is the Gaussian inhomogeneous broadening parameter expressed in frequency units.

4. Illustrative examples

The examples considered for illustration here are the same as those considered in [1] for the single-crystal case. In addition, they are generalized to cover polycrystalline case. The sample used is an irradiated malonic-acid crystal [13], wherein an unpaired electron spin $S = 1/2$, is in interaction with a single nucleus, $I = 1/2$, by hyperfine (HF) interaction, with the principal axes of the hyperfine (HF) matrix \tilde{A} and those of the \tilde{g} matrix assumed to be coincident. The orientations of the crystalline axes x, y, z are shown in Fig. 3, whose caption describes the angles (θ, ϕ) , which can be related to the Euler angles: $\eta = (\alpha, \beta, \gamma)$.

The details of the spin Hamiltonian and the basis vectors used are given in Appendix A. The values of the various parameters used are as follows: each $\pi/2$ pulse is of duration 5 ns; the nuclear Zeeman frequency $\omega_n = 14.5$ MHz; the principal values of the \tilde{g} and \tilde{A} matrices are: $\tilde{g} = (g_{xx}, g_{yy}, g_{zz}) = (2.0026, 2.0035, 2.0033)$; $\tilde{A} = (A_{xx}, A_{yy}, A_{zz}) = (-61.0 \text{ MHz}, -91.0 \text{ MHz}, -29.0 \text{ MHz})$; the Gaussian inhomogeneous broadening $\Delta = 4$ MHz for SECSY signal and $\Delta = 5$ MHz for echo-ELDOR signal.

The input values used for the parameters describing the relaxation matrix in the simulation of the time-domain signals are as follows (the same as those used in [1]): electron spin-spin relaxation time, $T_{2e} = 0.900 \mu\text{s}$; nuclear spin-spin relaxation time, $T_{2n} = 22 \mu\text{s}$; lattice-induced electron-spin flip relaxation rate, $W_e = 0.0167 \mu\text{s}^{-1}$; lattice-induced nuclear-spin flip relaxation rate, $W_n = 0.00714 \mu\text{s}^{-1}$; the cross relaxation rates involving simultaneous electron and spin flips $W_x = W_y = 0.00617 \mu\text{s}^{-1}$; the inverse Heisenberg exchange relaxation time, $\omega_{\text{HE}} = 0.0 \mu\text{s}^{-1}$.

The *single-crystal* SECSY and echo-ELDOR time-domain signal were calculated here for illustration for the orientation $(\theta, \phi) = (30^\circ, 0^\circ)$ in the zx -quadrant, so that $(\alpha, \beta, \gamma) = (0, -\theta, 0)$ [1] as shown in Figs. 4 and 5, respectively. The powder simulations are included in Figs. 6 and 7, respectively for SECSY and echo-ELDOR signals without Gaussian broadening, and in Figs. 8 and 9, respectively, with Gaussian broadening.

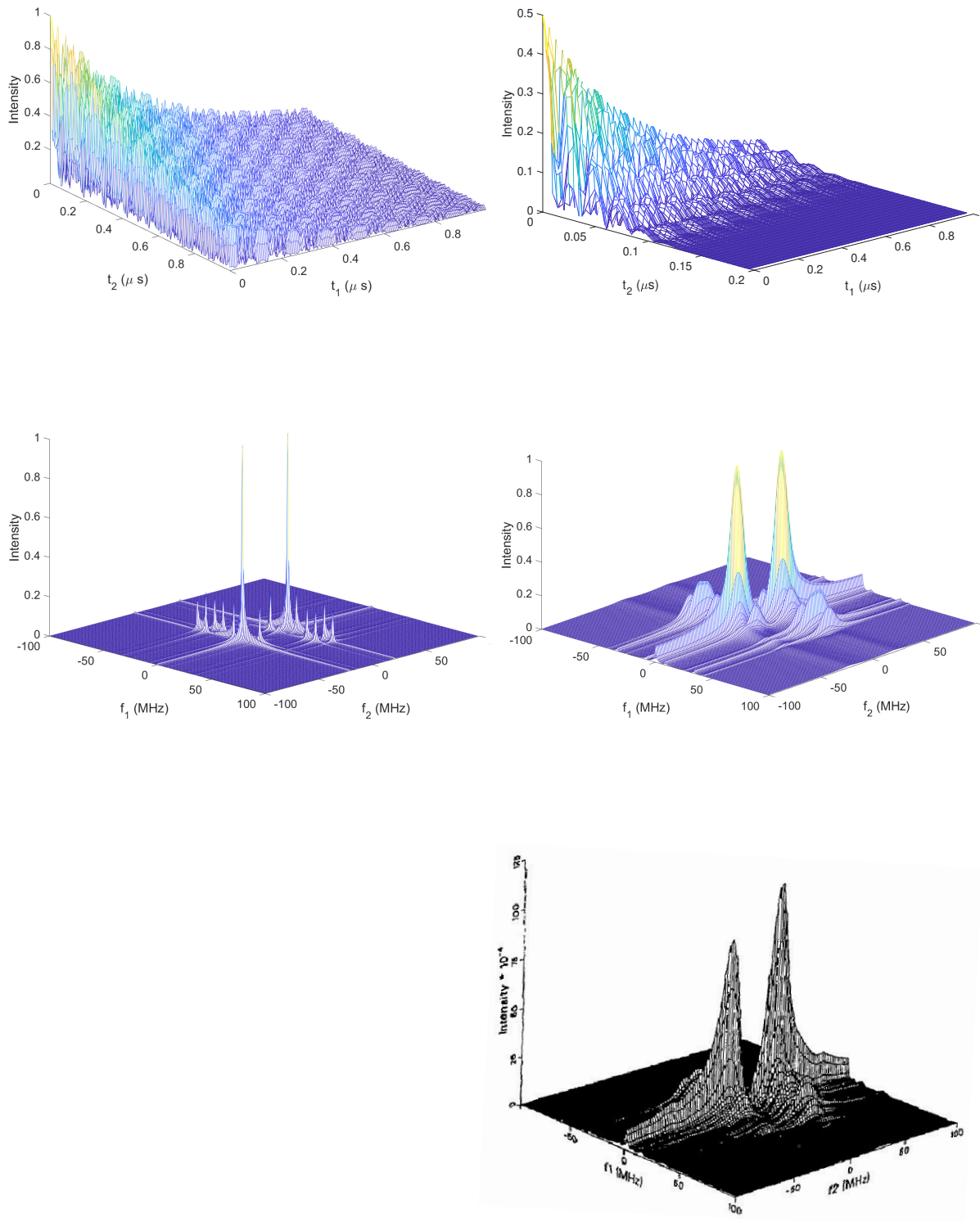


Figure 4. Simulated single-crystal SECSY time-domain signal with relaxation taken into account at $(\theta, \phi) = (30^\circ, 0^\circ)$ orientation of the external magnetic field with respect to the crystal axes in the zx quadrant [1], shown in the top row. The corresponding FT figures are shown in the second row. A Gaussian inhomogeneous broadening width $\Delta = 4$ MHz in accordance with [1] has been added along the t_2 axis in calculating the Fourier transform as shown in the right column for the time domain and FT signals. The corresponding SECSY experimental spectrum as extracted from LPF [1] is shown in the bottom row for comparison. It is reproduced with the permission of the authors [1].

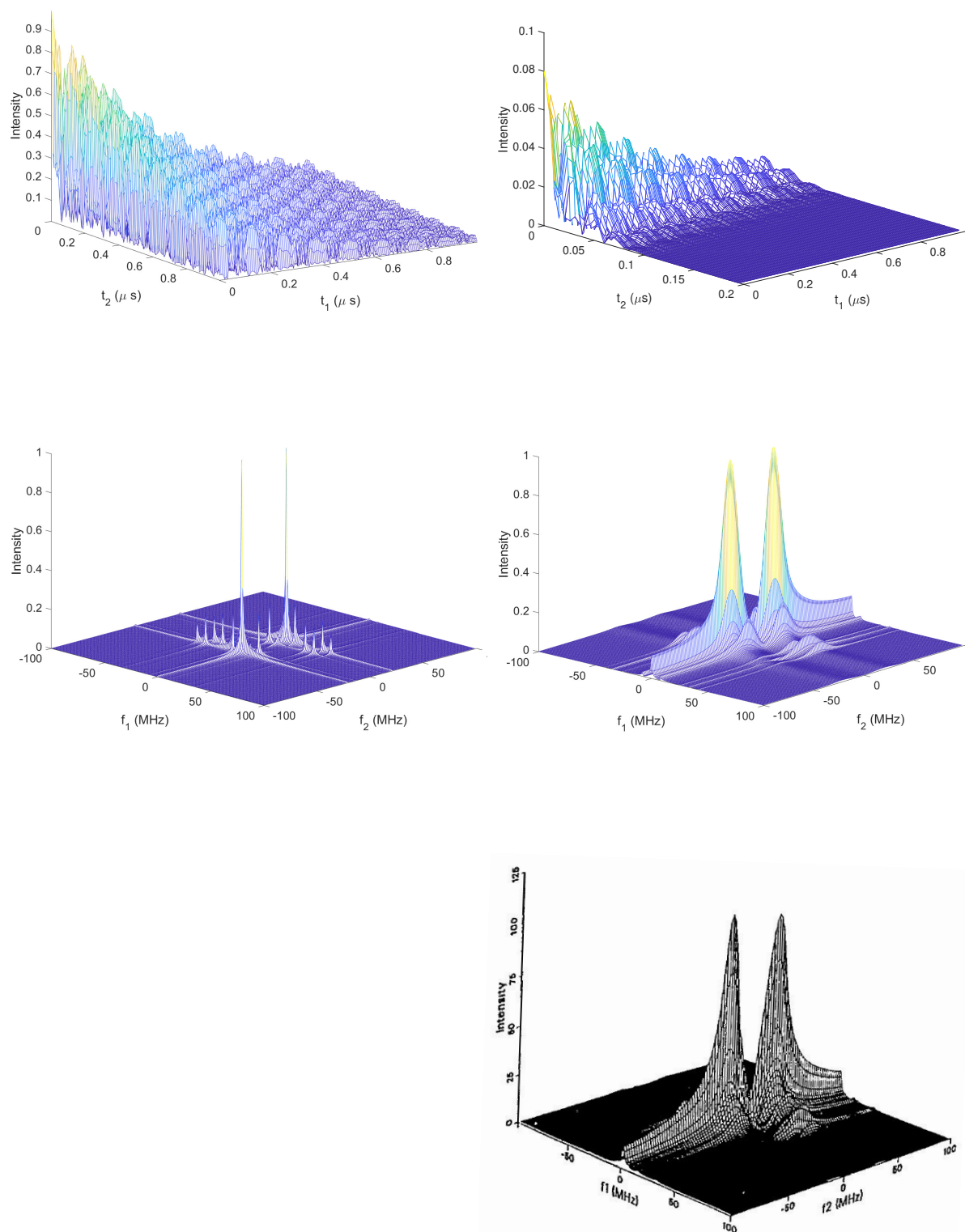


Figure 5. Simulated single-crystal echo-ELDOR time-domain signal with relaxation taken into account at $(\theta, \phi) = (30^\circ, 0^\circ)$ orientation of the external magnetic field with respect to the crystal axes in the zx quadrant [1], with the mixing times $T_m = 40 \mu s$, shown in the in the top row. The corresponding FT figures are shown in the second row. A Gaussian inhomogeneous broadening width $\Delta = 5$ MHz in accordance with [1] has been added along the t_2 axis in calculating the Fourier transform as shown in the right column for the time domain and FT signals. The corresponding echo-ELDOR experimental spectrum as extracted from LPF [1] is shown in the bottom row for comparison. It is reproduced with the permission of the authors [1].

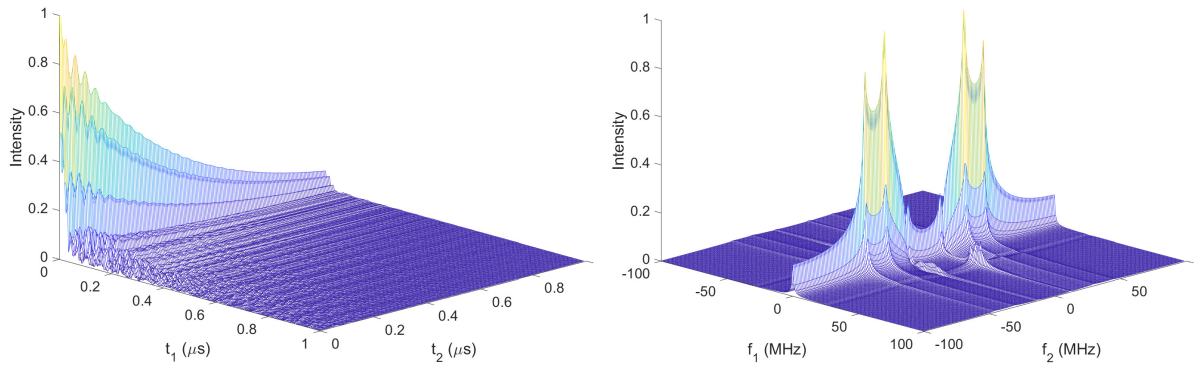


Figure 6. SECSY polycrystalline spectrum, for the (θ, ϕ) grid: $n_\theta = 90$, $n_\phi = 90$, without Gaussian inhomogeneous broadening. The simulated time-domain signal is shown on the left and the corresponding FT is shown on the right.

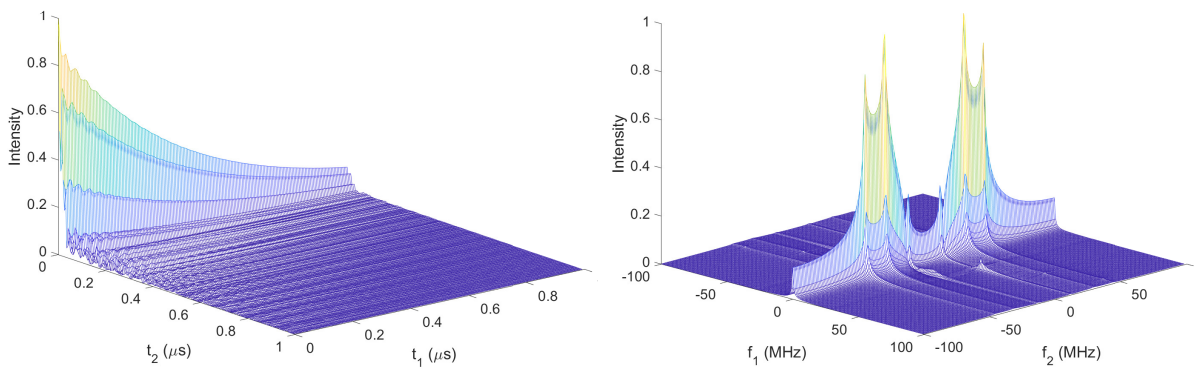


Figure 7. Echo-Eldor polycrystalline spectrum, for the (θ, ϕ) grid: $n_\theta = 90$, $n_\phi = 90$, without Gaussian inhomogeneous broadening. The simulated time-domain signal is shown on the left and the corresponding FT is shown on the right. The mixing time, T_m , as indicated in Fig. 2, is $40 \mu\text{s}$.

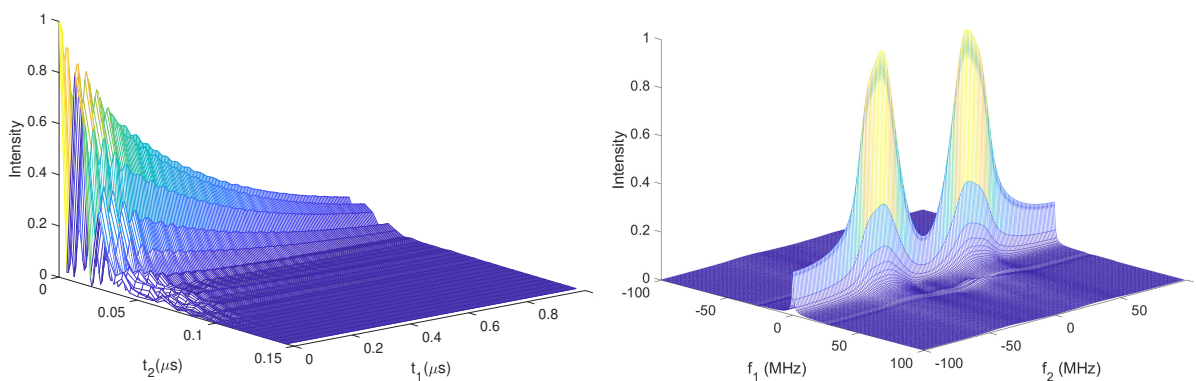


Figure 8. SECSY polycrystalline spectrum, for the (θ, ϕ) grid: $n_\theta = 90$, $n_\phi = 90$, with Gaussian inhomogeneous broadening of $\Delta = 4 \text{ MHz}$ added in accordance with [1]. The simulated time-domain signal is shown on the left and the corresponding FT is shown on the right.

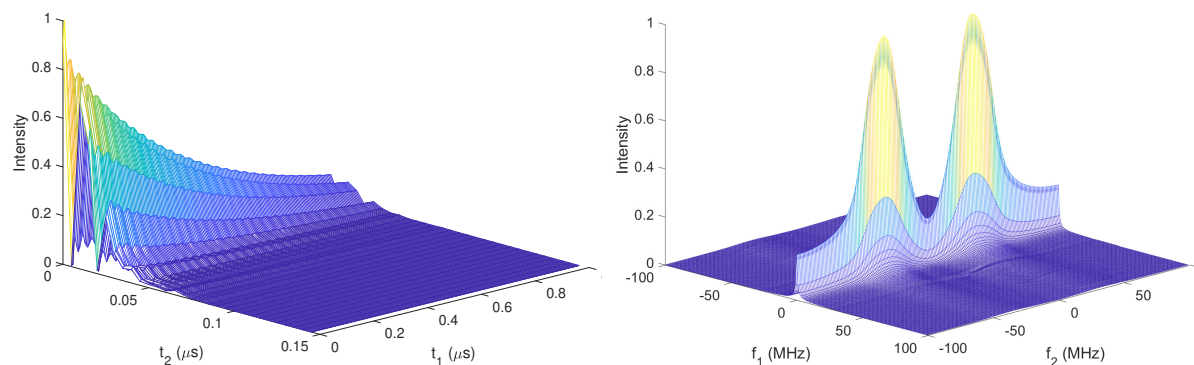


Figure 9. Eogo-ELDOR polycrystalline spectrum, for the (θ, ϕ) grid: $n_\theta = 90$, $n_\phi = 90$, with Gaussian inhomogeneous broadening of $\Delta = 5$ MHz added in accordance with [1]. The simulated time-domain signal is shown at the left and the corresponding FT is shown on the right. The mixing time, T_m , as indicated in Fig. 2, is $40 \mu\text{s}$.

5. Concluding remarks

This paper is devoted to a rigorous calculation of pulsed EPR signal in the presence of relaxation, providing a comprehensive theoretical treatment by numerically solving the LVN equation, including a detailed description of the relaxation processes as described by the Redfield theory [1]. The procedure of how to implement the theoretical approach numerically has been developed, and the applied algorithm and individual computational steps have been thoroughly discussed for a polycrystalline sample, and illustrated by examples.

The salient features of the present work are as follows.

1. An algorithm is developed here to calculate polycrystalline (powder) spectrum using MATLAB to calculate SECSY and echo-ELDOR pulsed-EPR signals for an electron-nuclear spin coupled system ($S = I = 1/2$) in an irradiated malonic-acid crystal.
2. These calculations can be easily carried out on a commonly available lap top equipped with Matlab within a reasonable time, on the order of 25-30 hours over a (θ, ϕ) grid of (90, 90) points.
3. The Matlab source code, see Misra and Salahi [15], can be modified to include any pulse sequences and any relaxation mechanism characterized by its particular matrix elements. Such an effort is in progress to take into account relaxation due to fluctuation of spin-Hamiltonian parameters due to spin-phonon modulation.

Acknowledgments

We are grateful to NSERC (Natural Sciences and Engineering Research Council of Canada) for financial support.

References

1. Lee S., Patyal B. R., Freed J. H. *J. Chem. Phys.* **98**, 3665 (1993).
2. Misra S. K., Li L. *J. Appl. Theol.* **2**, 5 (2018).
3. Gamliel D., Levanon H. *Stochastic Processes in Magnetic Resonance* (World Scientific, 1995).

4. Jeener J. “*Advances in Magnetic and Optical Resonance*” (Academic Press, 1982) Chap. Superoperators in Magnetic Resonance, pp. 1–51.
5. Redfield A. G. *IBM J. Res. Dev.* **1**, 19 (1957).
6. Gamliel D., Freed J. H. *Trans. Brit. Ceram. Soc.* **89**, 60 (1990).
7. Abragam A. *The Principles of Nuclear Magnetism* (Oxford University Press, 1961).
8. Aman K., Westlund P. O. *Phys. Chem. Chem. Phys* **9**, 691 (2007).
9. Hakansson P., Nguyen T., Nair P. B., Edge R., Stulz E. *Phys. Chem. Chem. Phys* **15**, 10930 (2013).
10. Schweiger A., Gunnar J. *Principles of Pulse Electron Paramagnetic Resonance* (Oxford University Press, 2001).
11. Deligiannakis Y., Louloudi M., Hadjiliadis N. *Coord. Chem. Rev.* **204**, 1 (2000).
12. Misra S. K., Borat P. P., Freed J. H. *App. Magn. Reson.* **36**, 237 (2009).
13. McConnell H. M., Heller C., Cole T., Fessenden R. W. *J. Am. Chem. Soc.* **82**, 766 (1960).
14. Misra S. K. *Multifrequency Electron Paramagnetic Resonance: Theory and Applications* (John Wiley & Sons, 2011).
15. Misra S. K., Salahi H. R. *J. Apl. Theol.* **3**, 9 (2019).
16. Freed J. H. “*Multiple Electron Resonance Spectroscopy*” (Springer, Boston, 1979) Chap. Theory of Multiple Resonance and ESR Saturation in Liquids and Related Media, pp. 73–142.
17. Freed J. H. *J. Chem. Phys.* **49**, 376 (1968).
18. Freed H. H. *J. Chem. Phys.* **43**, 1710 (1965).
19. Bain A. D. *J. Magn. Reson.* **56**, 418 (1984).
20. Bodenhausen G., Kogler H., Ernst R. R. *J. Magn. Reson.* **58**, 370 (1984).
21. Gemperle C., Aebli G., Schweiger A., Ernst R. R. *J. Magn. Reson.* **88**, 241 (1969).
22. Franck J. M., Chandrasekaran S., Dzikovski B., Dunnam C. R., Freed J. H. *J. Chem. Phys.* **142**, 212302 (2015).
23. Misra S. K., Freed J. H. “*Multifrequency Electron Paramagnetic Resonance: Theory & Applications*” (Wiley-VCH, Weinheim, 2011) Chap. Distance Measurements: Continuous-Wave (CW)-and Pulsed Dipolar EPR, pp. 545–588.
24. Stoll S., Kasumaj B. *Appl. Magn. Reson.* **35**, 15 (2008).

Appendices

A. Spin Hamiltonian for an electron-nuclear spin-coupled system in an irradiated malonic acid crystal

For the specific case of a single nucleus ($I = 1/2$) interacting with an unpaired electron ($S = 1/2$) by the hyperfine (HF) interaction, where the HF-interaction matrix has the principal axes coincident with those of the \tilde{g} matrix, the total Hamiltonian can be expressed as the sum of a static Hamiltonian and a pulse Hamiltonian [1]

$$\hat{H} = \hat{H}_0 + \hat{H}_1. \quad (\text{A.1})$$

In high-field approximation, nonsecular terms are negligible and static Hamiltonian can be written as:

$$\mathcal{H}_0 = \frac{\hat{H}_0}{\hbar} = CS_Z - \omega_n I_Z + AS_Z I_Z + \frac{1}{2}BS_Z I_+ + \frac{1}{2}B^*S_Z I_- \quad (\text{A.2})$$

which can be expressed in matrix form in $SzIz$ basis as:

$$\begin{pmatrix} (C - \omega_n + A/2)/2 & B/4 & 0 & 0 \\ B^*/4 & (C + \omega_n - A/2) & 0 & 0 \\ 0 & 0 & -(C + \omega_n + A/2) & -B/4 \\ 0 & 0 & -B^*/4 & (-C + \omega_n + A/2) \end{pmatrix}. \quad (\text{A.3})$$

The pulse Hamiltonian is:

$$\hat{H}_1(t) = \hat{\varepsilon}(t) = B_1 \gamma_e (S_x \cos(\phi) + S_y \sin(\phi)) \mathbb{1}_n = \frac{\omega}{2} (e^{-i\phi} S_+ + e^{i\phi} S_-) \mathbb{1}_n. \quad (\text{A.4})$$

In Eq. (A.4) B_1 is the amplitude of the microwave field, γ_e is the electron gyromagnetic factor, ω is the angular frequency of the microwave field and $\mathbb{1}_n$ is 2×2 unit matrix in nucleus space.

The coefficients in Eq. (A.2) in angular frequency units (Energy/ \hbar , where \hbar is Planck's constant divided by 2π) unit are expressed as follows [1]:

$$C = \frac{\beta_e B_0}{h} \left[\bar{g} + F \frac{1}{2} (3 \cos^2 \beta - 1) + F^{(2)} \sin^2 \beta \cos(2\gamma) \right], \quad (\text{A.5})$$

$$A = -2\pi \left[\bar{a} + D \frac{1}{2} (3 \cos^2 \beta - 1) + D^{(2)} \sin^2 \beta \cos(2\gamma) \right], \quad (\text{A.6})$$

$$B = -4\pi \left\{ D \frac{3}{4} \sin \beta \cos \beta - D^{(2)} \frac{1}{2} \sin \beta [\cos \beta \cos(2\gamma) - i \sin(2\gamma)] \right\} \quad (\text{A.7})$$

and

$$\bar{g} = \frac{1}{3} (g_{xx} + g_{yy} + g_{zz}), \quad (\text{A.8})$$

$$\bar{a} = \frac{1}{3} (A_{xx} + A_{yy} + A_{zz}). \quad (\text{A.9})$$

Here \bar{g} is the isotropic part of the \tilde{g} -matrix; \bar{a} is the isotropic part of the \tilde{A} -matrix. (It is noted that in LPF, there were misprints, which have been corrected in the above equations. In particular, insted of having the factors 2π in Eq. (A.6) and 4π in Eq. (A.7), there was a factor γ_e/\hbar in both places in LPF.)

$$F = \frac{2}{3} \left(g_{zz} - \frac{1}{2} (g_{xx} + g_{yy}) \right), \quad (\text{A.10})$$

$$D = \frac{2}{3} \left(A_{zz} - \frac{1}{2} (A_{xx} + A_{yy}) \right), \quad (\text{A.11})$$

$$F^{(2)} = \frac{1}{2} (g_{xx} - g_{yy}), \quad (\text{A.12})$$

$$D^{(2)} = \frac{1}{2} (A_{xx} - A_{yy}). \quad (\text{A.13})$$

Here ω_n is the nuclear Larmor frequency, $\Omega(\alpha, \beta, \gamma)$ are the Euler angles which describe the orientations of the principal axes of the \tilde{g} -matrix with respect to the static magnetic field and the principal axes of the hyperfine matrix \tilde{A} are assumed coincident with those of the matrix \tilde{g} . Since all the calculations are carried out in rotating frame, for which the effective field ($B = B_{\text{eff}} = 0$), the value of C in (A.5) becomes equal to zero as it is proportional to B .

B. Relaxation matrix elements according to Redfield theory

The effect of spin relaxation is taken into account to describe the rate of change of the density matrix as outlined by LPF, using the Redfield theory [1]:

$$\frac{d}{dt} \rho_{\alpha\alpha'}(t) = -i\omega_{\alpha\alpha'} \rho_{\alpha\alpha'} - \sum_{\beta\beta'} \hat{R}_{\alpha\alpha'\beta\beta'} (\rho_{\beta\beta'} - \rho_{0\beta\beta'}) \quad (\text{B.1})$$

with

$$\omega_{\alpha\beta} = E_{\alpha} - E_{\beta}, \quad (\text{B.2})$$

where E_{α}, E_{β} are the eigenvalues of the static Hamiltonian, \hat{H}_0 , for the electron-nuclear coupled system ($S = 1/2, I = 1/2$) as given by Eq. (A.2).

In Eq. (B.1), $\hat{R}_{\alpha\alpha'\beta\beta'}$ are the relaxation matrix elements, where $\alpha, \alpha', \beta, \beta'$ designate the eigenstates of the Hamiltonian \hat{H}_0 . The following specific values for the matrix elements, as given by Freed [16–18], are used here:

$$\hat{R}_{\alpha\beta, \alpha\beta} = -\left(\frac{1}{T_2}\right)_{\alpha\beta}, \quad (\text{B.3})$$

$$\hat{R}_{\alpha\alpha, \beta\beta} = W_{\alpha\beta}, \quad (\text{B.4})$$

$$\hat{R}_{\alpha\alpha, \alpha\alpha} = -\sum_{\gamma \neq \alpha} W_{\alpha\gamma}. \quad (\text{B.5})$$

Otherwise

$$\hat{R}_{\alpha\beta, \zeta\eta} = 0. \quad (\text{B.6})$$

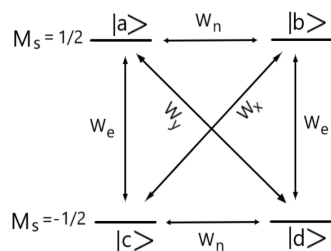
The relaxation pathways among the various eigenstates of the coupled electron-nuclear spin system in the lattice, as defined in the H_0 basis [16], are shown in the figure below, where $|a\rangle$ and $|b\rangle$ indicate the nuclear sublevels coupled to the electronic magnetic quantum number $M_S = 1/2$ and $|c\rangle$ and $|d\rangle$ indicate the nuclear sublevels coupled to the electronic magnetic quantum number of $M_S = -1/2$. It is assumed, with reference to the above diagram, that [1]

$$W_{ab} = W_{ba} = W_{cd} = W_{dc} = W_n, \quad (\text{B.7})$$

$$W_{ac} = W_{ca} = W_{bd} = W_{db} = W_e, \quad (\text{B.8})$$

$$W_{ad} = W_{da} = W_y, \quad (\text{B.9})$$

$$W_{bc} = W_{cb} = W_x \quad (\text{B.10})$$



and

$$(T_2)_{ac} = (T_2)_{bd} = (T_2)_{ad} = (T_2)_{bc} = T_{2e}, \quad (\text{B.11})$$

$$(T_2)_{ab} = (T_2)_{cd} = T_{2n}. \quad (\text{B.12})$$

All matrix elements $\hat{R}_{\alpha\beta,\zeta\eta} = 0$, except for the non-zero elements of the relaxation matrix corresponding to the above diagram, as obtained from Eqs.(B.3) -(B.6)), which are [1]:

$$\hat{R}_{ab,ab} = \hat{R}_{ba,ba} = \hat{R}_{cd,cd} = \hat{R}_{dc,dc} = -\frac{1}{T_{2n}}, \quad (\text{B.13})$$

$$\hat{R}_{ac,ac} = \hat{R}_{ca,ca} = \hat{R}_{ad,ad} = \hat{R}_{da,da} = \hat{R}_{bc,bc} = \hat{R}_{cb,cb} = \hat{R}_{bd,bd} = \hat{R}_{db,db} = -\frac{1}{T_{2e}}, \quad (\text{B.14})$$

$$\hat{R}_{aa,aa} = \hat{R}_{dd,dd} = -W_e - W_n - W_y, \quad (\text{B.15})$$

$$\hat{R}_{bb,bb} = \hat{R}_{cc,cc} = -W_e - W_n - W_x, \quad (\text{B.16})$$

$$\hat{R}_{aa,bb} = \hat{R}_{bb,aa} = \hat{R}_{cc,dd} = \hat{R}_{dd,cc} = W_n + \frac{\omega_{\text{HE}}}{4}, \quad (\text{B.17})$$

$$\hat{R}_{aa,cc} = \hat{R}_{bb,dd} = \hat{R}_{cc,aa} = \hat{R}_{dd,bb} = W_e + \frac{\omega_{\text{HE}}}{4}. \quad (\text{B.18})$$

Here $\omega_{\text{HE}} = 0$ as used by LPF [1].

C. Coherence pathways

A coherence pathway is the sequence of coherence orders through which the magnetization evolves during a pulse sequence. All experiments start with zero order coherence (z -magnetization) and end with a coherence order of -1 , which is by convention the one that is detected by the quadrature detector. Without quadrature detection the $+1$ -coherences would be equally detectable. It is noted that all higher orders are not correlated with the observable magnetization.

The selection of the appropriate coherence pathways can be experimentally achieved by phase cycling, or by the use of pulsed field gradients [19–21]. The properties of the RF-pulses, e.g. flip angle, offset effects, inhomogeneity, require a weighting over the different coherence transfer pathways [9, 12, 22]. The coherence pathways S_{c-} for obtaining SECSY and echo-ELDOR signals, used commonly, are depicted in Figs. 1 and 2, respectively.

Selection of coherent pathways by appropriate selection of the corresponding elements of the density matrix. For single electron-nuclear coupled system with electron spin $S = 1/2$, nuclear spin $I = 1/2$, the dimension of the coupled spin Hamiltonian is $(2S_1 + 1) \otimes (2I_1 + 1) = 4$, so that the density matrix in the electron-nuclear spin-coupled direct product space the total density matrix $\rho = \rho_e \otimes \rho_n$, where ρ_e and ρ_n are, respectively, the density matrices in the electronic and nuclear subspaces, In the following, the coherence order p represents the transverse magnetization corresponding to the spins rotating in a plane perpendicular to the external field [23, 24]. The matrix elements for the various coherence orders are defined as follows, which will be consistent with the experimental technique to acquire a particular coherent pathway.

- For the pathway with the coherence order $p = 1$, all matrix elements of the density matrix, ρ_e , are put equal to zero, except for those corresponding to $\rho_e(1,2)$.
- For the pathway with the coherence order $p = 0$, all matrix elements of the density matrix, ρ_e , are put equal to zero, except for those corresponding to $\rho_e(1,1)$ and $\rho_e(2,2)$.
- For the pathway with the coherence order $p = -1$, all matrix elements of the density matrix, ρ_e , are put equal to zero, except for those corresponding to $\rho_e(2,1)$.

D. The relationship between (α, β, γ) and (θ, ϕ)

The spin Hamiltonian (A.2) is expressed in the principal-axes system of the magnetic matrices \tilde{g} and \tilde{A} (xyz ; Fig. 3), assumed to be coincident with each other. It will, therefore, be convenient for calculating powder average to carry out integration using the Euler angles (β, γ) , instead of the angles (θ, ϕ) as is usually done for powder averaging over the unit sphere. In order to transform the laboratory coordinate system (XYZ ; where Z is in the direction of the external magnetic field) to the principal-axes system of the magnetic matrices \tilde{g} and \tilde{A} (xyz) one needs, in general, three Euler angles (α, β, γ) . When there is no restriction on choosing the orientations of the axes X and Y , as is the present case, it is always possible to set the first Euler angle to zero ($\alpha = 0$), which is required for the discussion that follows. In order to set α equal to 0, one needs to choose the Y axis along the line of nodes, defined by the intersection of the xy and XY planes, using the convention in LPF, i.e. right-handed coordinate system, counterclockwise rotations and choosing second rotation around the new Y axis. Now, one only needs two rotations to bring in coincidence Z to z and X to x . The relationship between the angles (β, γ) and (θ, ϕ) is found to be different in different octants, as given in Table 1, which also defines the quadrants ①-⑧.

Table 1. The relationship between (β, γ) and (θ, ϕ) in the different quadrants indicated as 1-8

	$0 \leq \theta < \pi/2$	$\pi/2 \leq \theta < \pi$
$0 \leq \phi < \pi/2$	$\beta = -\theta, \gamma = -\phi$ ①	$\beta = \theta, \gamma = \pi - \phi$ ⑤
$\pi/2 \leq \phi < \pi$	$\beta = \theta, \gamma = \pi - \phi$ ②	$\beta = -\theta, \gamma = -\phi$ ⑥
$0 \leq \phi < \pi/2$	$\beta = -\theta, \gamma = -\phi$ ③	$\beta = \theta, \gamma = \pi - \phi$ ⑦
$\pi/2 \leq \phi < \pi$	$\beta = \theta, \gamma = \pi - \phi$ ④	$\beta = -\theta, \gamma = -\phi$ ⑧

One can substitute β for θ and γ for ϕ , to calculate the powder average done over all possible angles (θ, ϕ) on the unit sphere, that includes the quadrants ①-⑧ as defined in Table 1. This is possible because of the following facts: (i) the relationships between (β, γ) and (θ, ϕ) given in Table 1; (ii) the equivalence of the eigenvalues and eigenvectors of the spin Hamiltonian given by Eq. (A.2) for quadrants ① and ② to those in quadrants ③-⑧. This is seen as follows: For any (β, γ) in quadrant ①, there exist sets of (β, γ) in each of the quadrants ③, ⑥ and ⑧, which have the same eigenvalues and eigenvectors of the spin Hamiltonian given by Eq. (A.2). The same relationship of the eigenvalues and eigenvectors holds true for quadrant

② with the quadrants ④, ⑤ and ⑦. It is noted that both the eigenvalues and eigenvectors in the powder calculation are required in order to transform the Liouvillian as given by Eq. (7) to the eigenvalues basis from that in the $S_Z I_Z$ basis as given in Eq. (A.3) to take into account the relaxation matrix in the eigenvalue basis, given by Eqs. (B.3)-(B.6); However, integration over only the top quarter sphere: $\beta[0, \pi/2]$ and $\gamma[0, \pi]$, that is over the quadrants ① and ② is required, since the integration over each of the remaining three quarter spheres to cover the entire sphere will give the same result as found by the equivalence argument given above. This simplification reduces the time required to carry out the calculation by the factor of 4.

E. Flow chart

